Supplementary Information (SI) for Journal of Materials Chemistry A.

Micro-sized Conductive Metal-organic Frameworks Nanosheet for Electrochemical Hydrogen Evolution Reaction in Acidic Media

Yahan Wang,[1,#] Jinna Wang,[1,#] Junfeng Zeng,[1,#] Hongli Zhu,[1] Heng Chu,[1] Yan Zhang,[1,*] Hussein A. Younus,[3] Wenpeng Ni[1,2,4,*] and Shiguo Zhang,[1,*]

1 College of Materials Science and Engineering, Hunan University, Changsha 410082, China.
2 Research Institute of Hunan University in Chongqing, Chongqing 401120, China
3 Chemistry Department, Faculty of Science, Fayoum University, Fayoum 63514, Egypt
4 Greater Bay Area Institute for Innovation, Hunan University, Guangzhou, 511340, China

Corresponding authors: zyan1980@hnu.edu.cn, aniwenpeng@163.com, zhangsg@hnu.edu.cn

Experimental Section

Materials synthesis

Synthesis of M-HITP nanoparticles: Nickel acetate (0.17 mM) was dissolved in 18 mL of dimethyl sulfoxide and stirred at 25 °C for 30 min. Subsequently, 0.17 mM of 2,3,6,7,10,11-hexaaminotriphenylene (HITP) dissolved in 18 mL of deionized water was added, followed by 24 mL of sodium acetate solution (4 M). The resulting mixture was transferred into a 100 mL Teflon-lined autoclave and heated at 100 °C for 16 h. After cooling to room temperature, the solid product was collected by centrifugation, washed thoroughly with deionized water and methanol, and dried under vacuum at 60 °C to yield M-HITP nanoparticles.

Synthesis of M-HITP nanosheets: M-HITP nanoparticles (25 mg, M = Ni, Co, or CoNi) were dispersed in 1 mL of 25 wt% aqueous tetramethylammonium hydroxide (TMAH) solution and subjected to sonication at 40 kHz for 20 h. The suspension was subsequently diluted with 50 mL of deionized water, dialyzed, and centrifuged at 10,000 rpm. The supernatant was collected and freeze-dried to afford M-HITP nanosheets.

Physical characterization

Deionized water (18.2 MΩ·cm) was supplied by an ultrapure purification system (Master-S15Q, Hitech Instruments Co., Ltd., Shanghai, China). Phase identification was carried out on a D/max 2550 VB X-ray diffractometer employing Cu Kα radiation (λ = 0.154 nm) with a scanning rate of 10° min^{-1}. X-ray photoelectron spectroscopy (XPS) was recorded on an ECSALAB250Xi spectrometer using Al Kα radiation (1486.6 eV), and the binding energies were calibrated against the C 1s peak at 284.6 eV. Surface morphologies were observed by field-emission SEM (Hitachi S-4800), while high-resolution TEM (Titan G2 60-300) equipped with a spherical aberration corrector and EDS mapping was employed for microstructural characterization. Nitrogen adsorption–desorption isotherms were measured at 76.2 K on a volumetric analyzer (JW-BK200C, Beijing JWGB Sci. & Tech. Co., Ltd.), and pore size distributions were derived from the adsorption branch using nonlocal density functional theory (NLDFT). Raman spectra were obtained with a DXR i Raman Microscope (Thermo Fisher) under a 532 nm laser. Electrical conductivity of the powders was tested by the four-probe method (ST2722 Powder Resistivity Tester, Suzhou Lattice Electronics Co., Ltd.).

Electrochemical test

All electrochemical characterizations were carried out on a potentiostat using a conventional three-electrode setup, consisting of a rotating disk electrode (RDE, 5 mm diameter) as the working electrode, an Ag/AgCl electrode (3.5 M KCl) as the reference, and a Pt mesh (1 cm^2) as the counter electrode. The electrolyte was 0.5 M H_2SO_4 saturated with Ar. Measurements were recorded on a Biologic electrochemical workstation with 85% iR compensation, and all potentials were converted to the reversible hydrogen electrode (RHE) scale. Catalyst inks were prepared by dispersing 5 mg of catalyst powder in 950 µL of ethanol and 50 µL Nafion solution (5 wt%), followed by sonication for 30 min. The catalyst loading on the RDE was controlled at 0.2 mg cm^{-2}. Linear sweep voltammetry

(LSV) was performed at a scan rate of 10 mV s^{-1} without rotation. Double-layer capacitance (C_{dl}) was determined from cyclic voltammetry (CV) curves collected in the non-Faradaic region (open circuit potential ± 50 mV) with scan rates from 2 to 10 mV s^{-1}; C_{dl} values were extracted from the slope of the current density versus scan rate plot. The electrochemically active surface area (ECSA) was calculated using ECSA = C_{dl} / C_s, with C_s = 40 μF cm^{-2} for a flat electrode. Electrochemical impedance spectroscopy (EIS) was conducted at fixed potentials over a frequency range of 0.1 Hz to 1 MHz with a 5 mV AC perturbation.

Theoretical calculations

All density functional theory (DFT) calculations were performed using the Vienna Ab-initio Simulation Package (VASP).[1,2] The exchange-correlation functional was described by the Perdew-Burke-Ernzerhof (PBE) parametrization within the generalized gradient approximation (GGA). The projector-augmented wave (PAW) method was employed to treat the core-valence electron interactions.[3,4] Spin-polarized calculations were conducted with initial magnetic moments of 3 μB for Co and 2 μB for Ni atoms. Van der Waals dispersion corrections (DFT-D3 method [5]) were included in all calculations to ensure an accurate representation of weak intermolecular interactions. The plane-wave kinetic energy cutoff was set to 500 eV. Brillouin zone sampling was conducted using Monkhorst-Pack k-point grids of 2×2×1 for structural optimizations and 6×6×1 for electronic structure calculations. The computational supercell was constructed with lattice parameters of a = 21.89 Å, b = 18.96 Å, and c = 20 Å, with angles α = β = 90° and γ = 120°. To eliminate spurious interactions between periodic images, a vacuum layer of 20 Å was applied along the z-axis direction. To account for the aqueous electrolyte environment in electrocatalytic processes, implicit solution effects were incorporated using the VASPsol package.[6] The solvent dielectric constant (E_{B}_k) is assigned a value of 78.36. Geometric optimizations were performed until the total energy converged to within 10^{-5} eV and all atomic forces were less than 0.02 eV/Å. All optimized structures were visualized using the VESTA software package.[7]

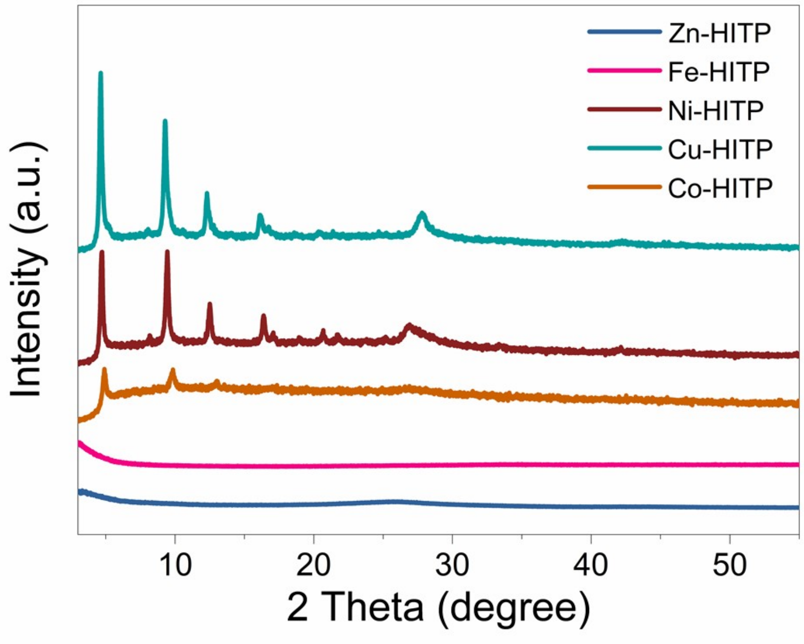

Figure S1. XRD patterns of Zn-, Fe-, Ni-, Cu-, and Co-HITP nanoparticles.

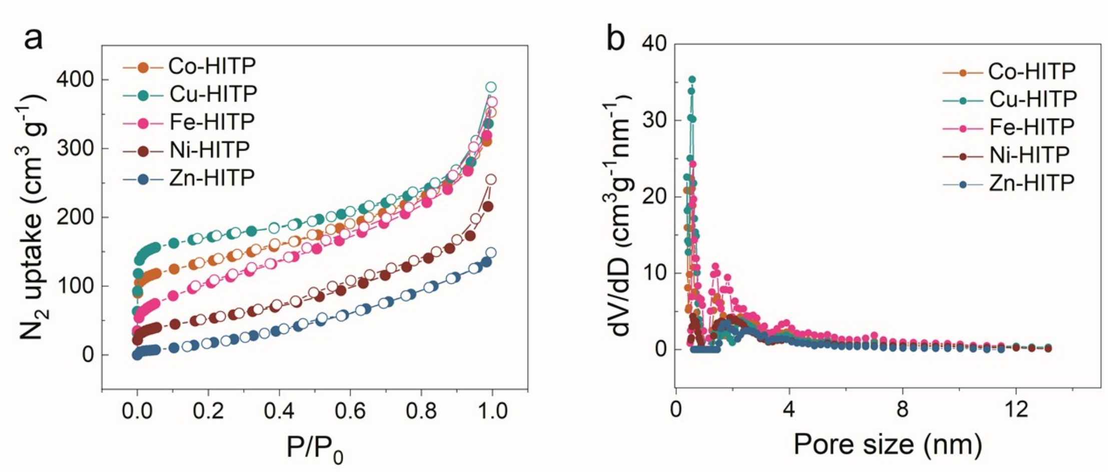

Figure S2. (a) N_2 sorption isotherms at 77 K. (b) The corresponding pore size distribution curves of Co-, Cu-, Fe-, Ni-, and Zn-HITP.

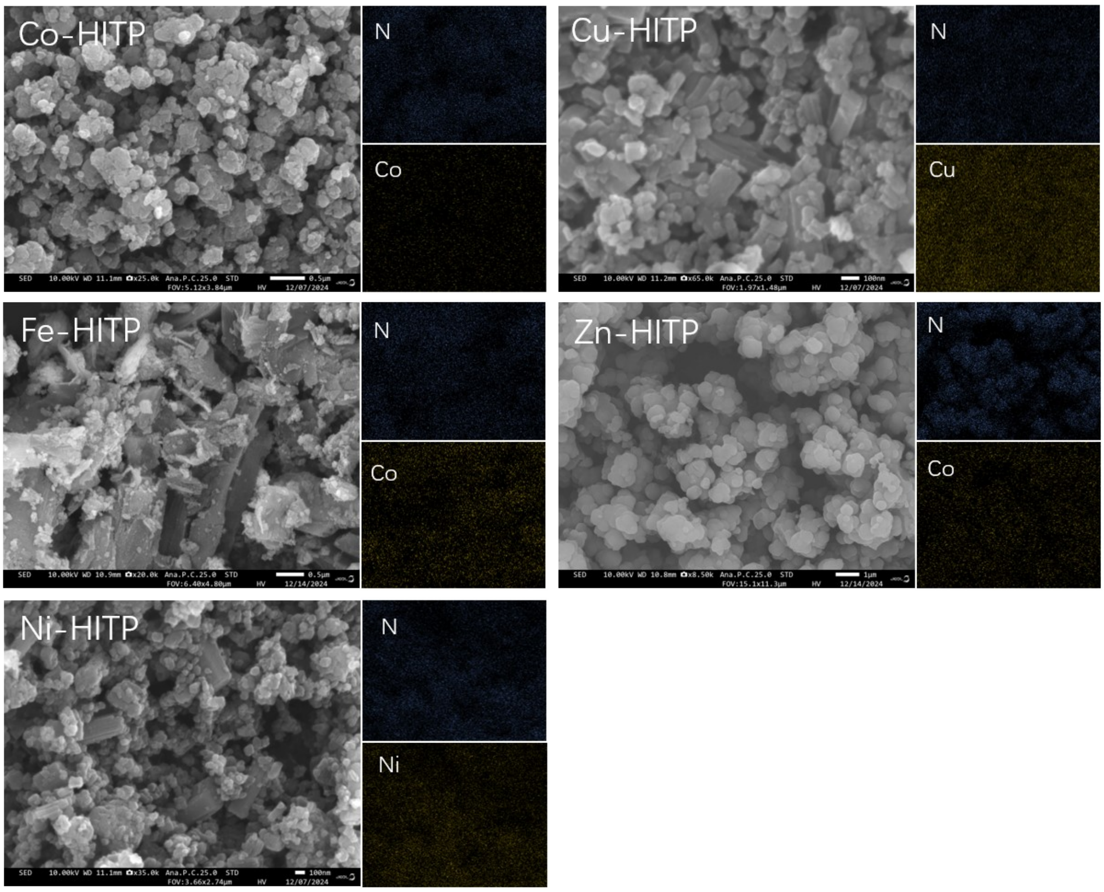

Figure S3. The SEM images of Co-, Cu-, Fe-, Zn-, and Ni-HITP.

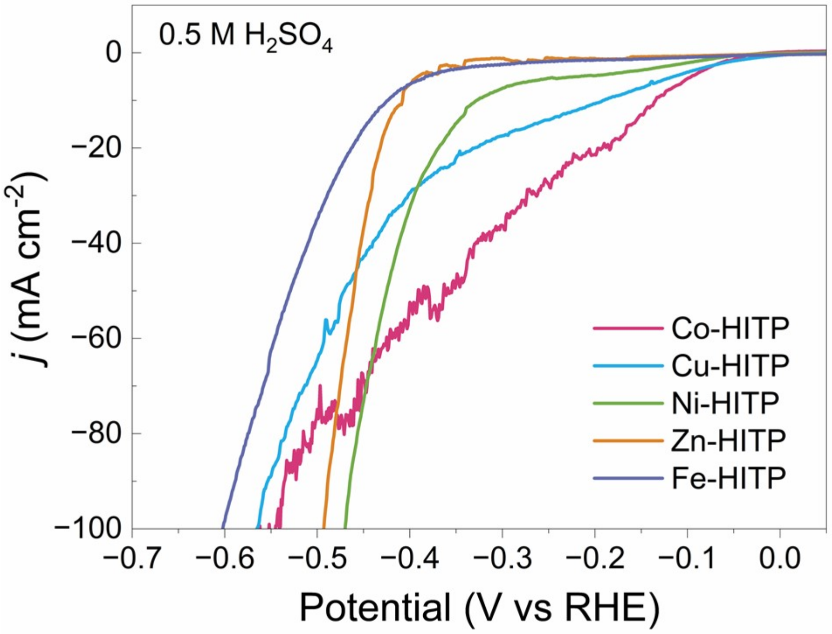

Figure S4. The LSV curves of M-HITP (M=Co, Cu, Ni, Zn, Fe) collected in 0.5 M H_2SO_4 electrolyte.

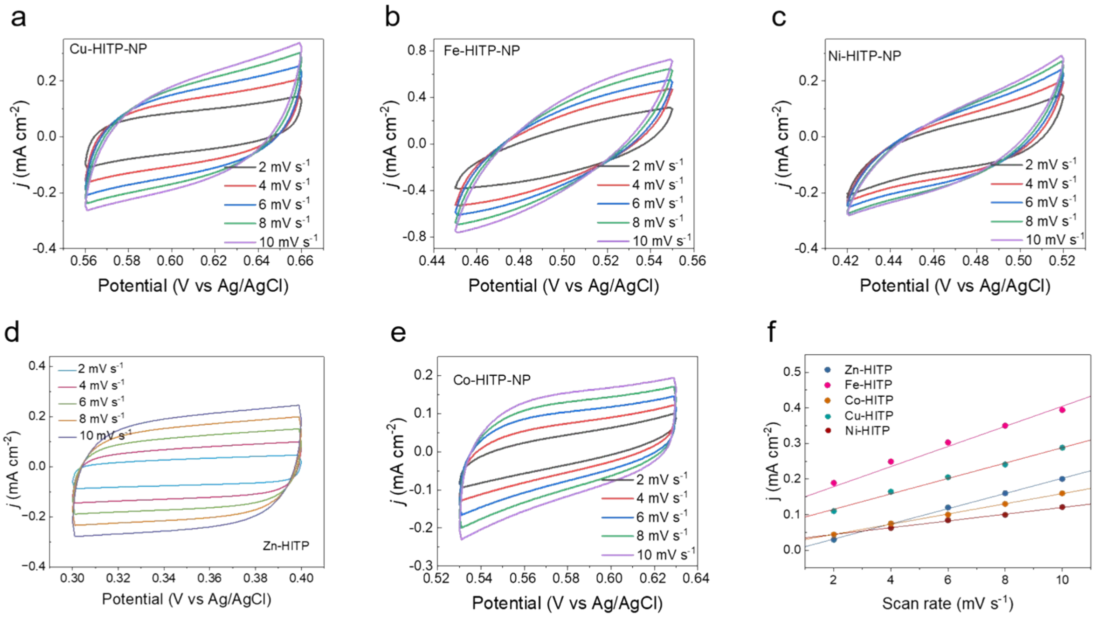

Figure S5. The CV curves of (a) Cu-HITP NP, (b) Fe-HITP NP, (c) Ni-HITP NP, (d) Zn-HITP NP, and (e) Co-HITP NP obtained in the non-Faradaic potential window. (f) The dependence of j on the scan rate for Cu-, Fe-, Ni-, Zn-, and Co-HITP NP.

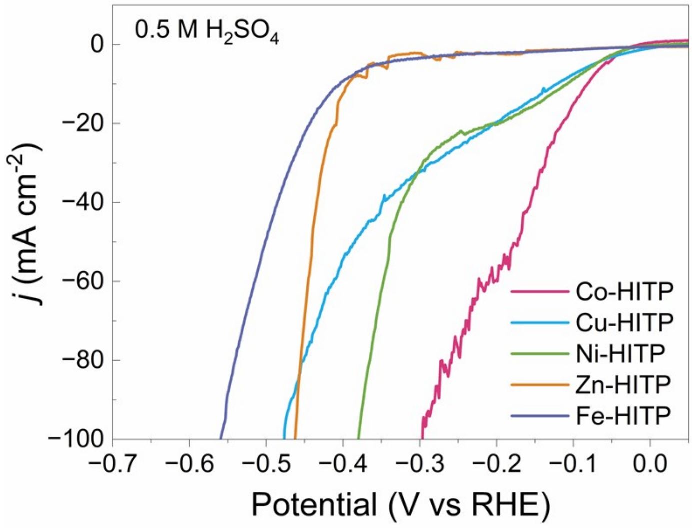

Figure S6. The ECSA-normalized LSV curves for Co-, Cu-, Ni-, Zn-, and Fe-HITP NP.

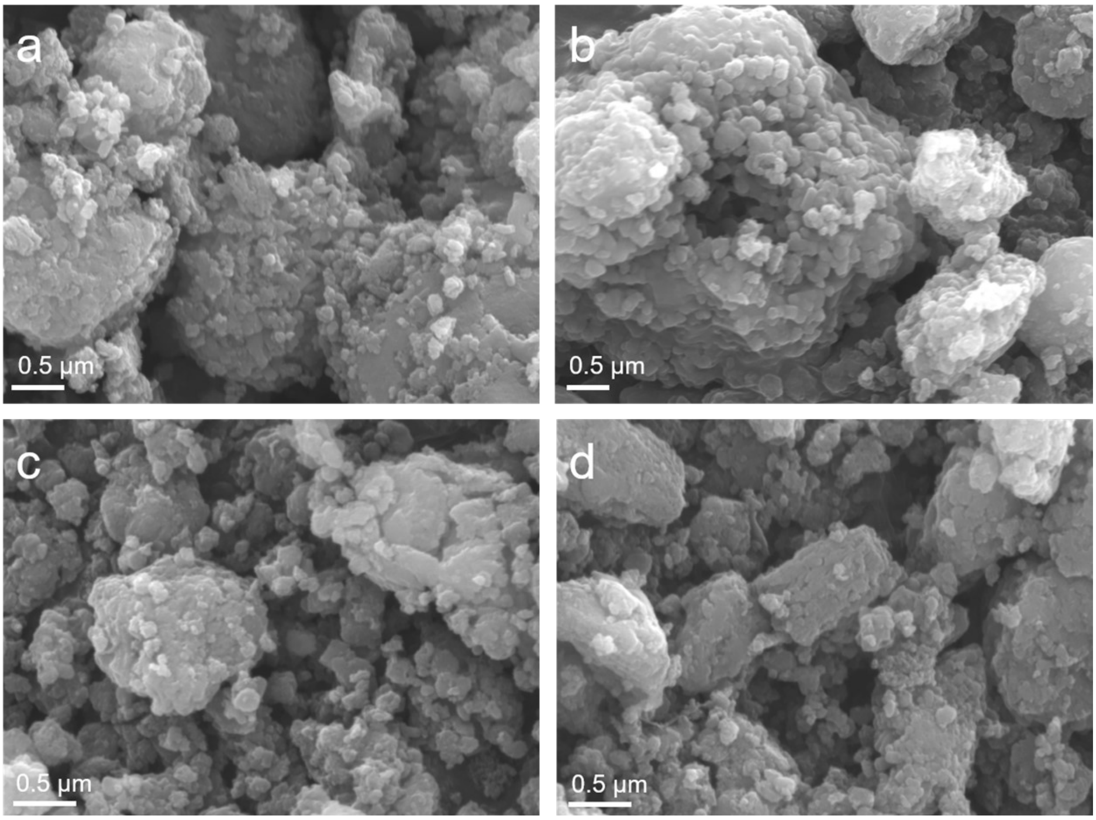

Figure S7. The SEM images of Ni-HITP after sonication in NaOH aqueous solution (pH=13) for (a) 10 min, (b) 20 min, (c) 1 h, and (d) 2 h.

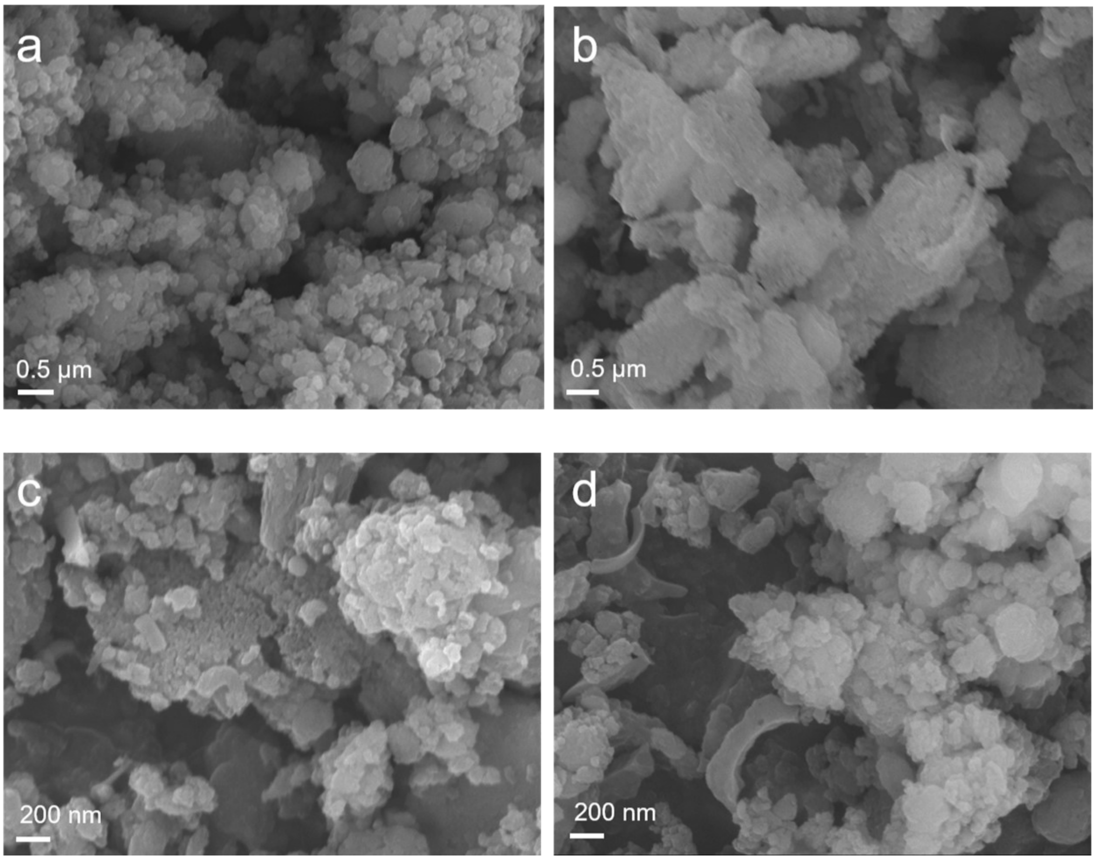

Figure S8. The SEM images of Ni-HITP after sonication in tetraethylamine hydroxide aqueous solution for (a) 10 min, (b) 20 min, (c) 1 h, and (d) 2 h.

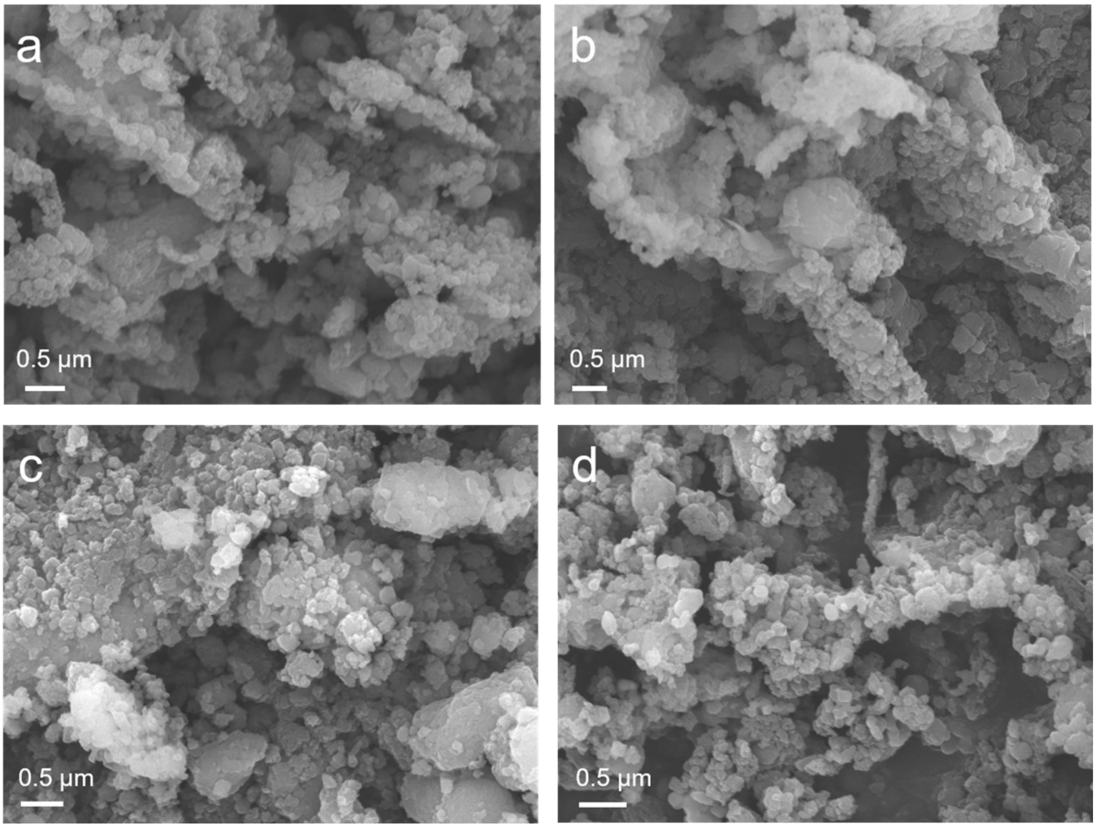

Figure S9. The SEM images of Ni-HITP after sonication in tetrabutylamine hydroxide aqueous solution for (a) 10 min, (b) 20 min, (c) 1 h, and (d) 2 h.

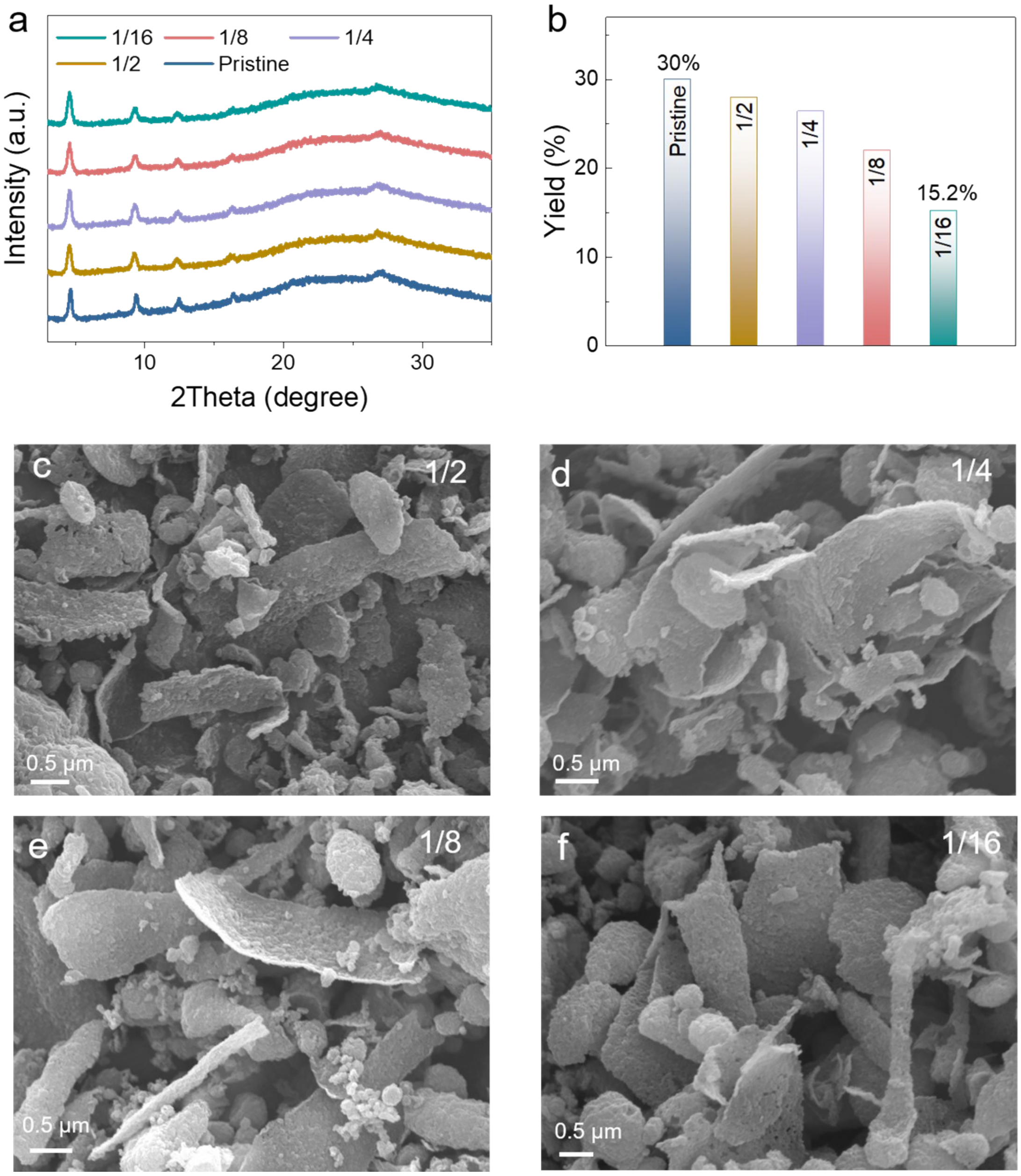

Figure S10. (a) XRD patterns, (b) Product yield for Ni-HITP NS collected by sonication in tetramethylammonium hydroxide aqueous solution with different concentrations. The SEM image of Ni-NITP NS that was produced by sonication in tetramethylammonium hydroxide aqueous solution diluted by (c) 2-fold, (d) 4-fold, (e) 8-fold, (f) 16-fold.

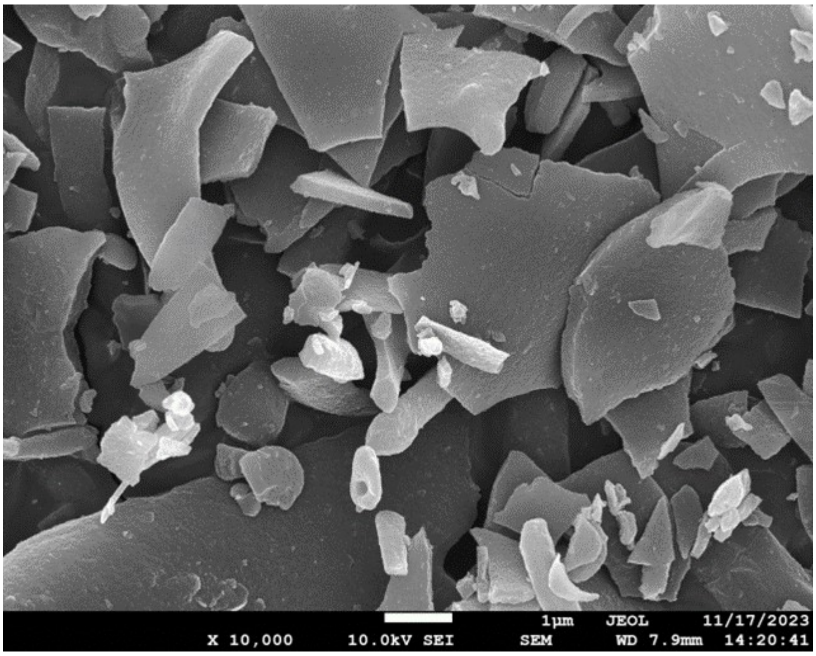

Figure S11. The SEM image of Ni-HITP after magnetic stirring for 20 h in tetramethylammonium hydroxide aqueous solution.

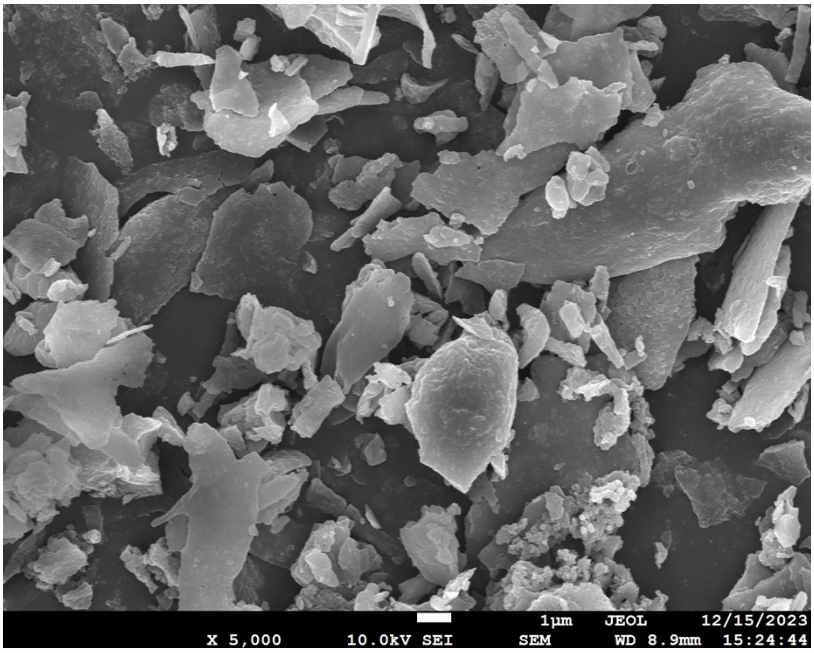

Figure S12. The SEM image of Ni-HITP after probe sonication for 20 h in tetramethylammonium hydroxide aqueous solution.

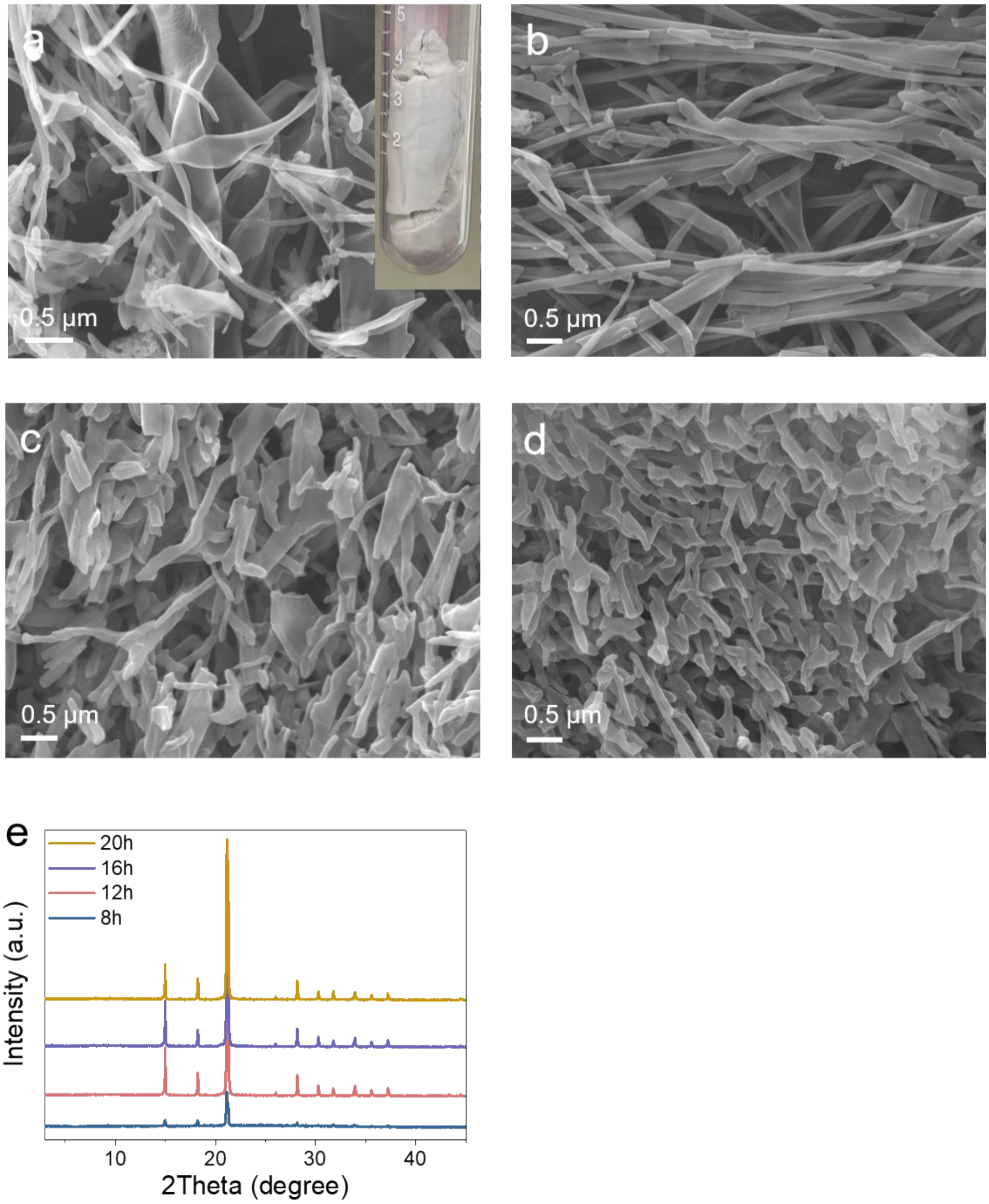

Figure S13. The Ni-HITP assembly after sonication in tetramethylammonium perchlorate for (a) 8 h, (b) 12 h, (c) 16 h, and (d) 20 h, as well as (e) the corresponding XRD patterns. The inset of (a) is the photo image of the sample after 8 h of sonication.

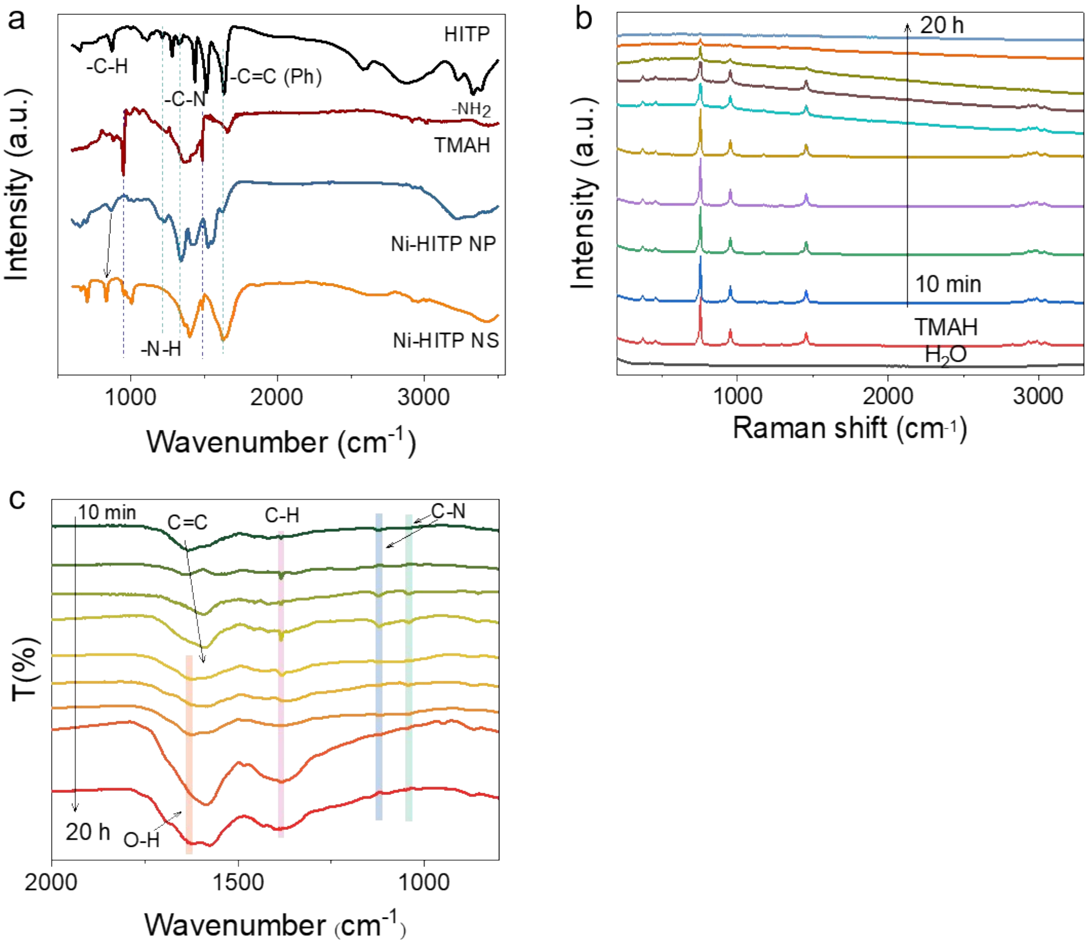

Figure S14. (a) The FTIR of HITP, TMAH, Ni-HITP NP, and Ni-HITP NS. (b) Raman spectra of the liquor after centrifugation. (c) FTIR of Ni-HITP samples collected after sonication for different times (10 min, 20 min, 1 h, 2 h, 4 h, 8 h, 12 h, 16 h, and 20 h).

We conducted the FTIR measurements for tracking the structural evolution during sonication treatment of Ni-HITP NP. As shown in **Figure S14a**, the FTIR spectrum of the HITP ligand exhibits characteristic peaks corresponding to the C–N bond, C=C bond in phenyl moieties, C–H stretching in the aromatic ring, and the –NH_2 group, appearing at 1337 cm^{-1}, 1437 cm^{-1} (and 1634 cm^{-1}), 872 cm^{-1}, and 3300 cm^{-1}, respectively. In the Ni-HITP NS sample, the signals associated with C–N, C=C, and C–H bonds remain distinguishable; however, a broad peak emerges above 3000 cm^{-1}, accompanied by the disappearance of the distinct –NH_2 peak, indicating the coordination interaction between the –NH moiety and Ni atoms. Upon sonication treatment in tetramethylammonium hydroxide (TMAH), the N–H stretching vibration completely vanished, confirming the deprotonation of the –NH moieties in Ni-HITP NS. Meanwhile, the FTIR spectrum of Ni-HITP NS revealed new peaks at 951 cm^{-1} and 1486 cm^{-1}, attributable to TMAH, as well as a red shift of the C–H stretching peak. These observations collectively demonstrate the ligand deprotonation and incorporation of TMAH into the final nanosheet structure.

Subsequently, we monitored the time-resolved evolution of Ni-HITP NP during sonication, along with the molecular variations in the residual liquor after centrifugation. Particular attention was given to the first two hours of sonication, during which the rearrangement of Ni-HITP NPs occurred, as revealed by SEM observations. In the Raman spectra of the residual liquor collected during this period (**Figure S14b**), only peaks corresponding to TMAH were detected, with no discernible signals from the HITP ligand, thereby excluding any ligand leaching during the rearrangement process. Meanwhile, the FTIR spectra of the collected solids (**Figure S14c**) exhibit weak peaks corresponding to the C–H stretching and C–N bonds of TMAH, confirming the partial incorporation of TMAH into the Ni-HITP framework during the rearrangement step. This finding aligns with the conclusion that TMAH cations mediate the reorganization of Ni-HITP NPs. Furthermore, the C=C stretching vibration of the HITP ligand shows a red shift from 1638 cm^{-1} to 1585 cm^{-1}, indicative of reduced C=C bond strength. This phenomenon can be rationalized by the enhanced coordination interaction between Ni atoms and N sites, which weakens the C=C bonding within the phenyl rings.

We next focused on the subsequent 18 hours of sonication. In the Raman spectra of the residual liquor, the intensity of TMAH-related peaks gradually diminished after 2 hours of treatment, which can be attributed to the progressive consumption of TMAH during the reconstruction of Ni-HITP. The TMA^+ cations were likely adsorbed onto the surface or within the pores of the forming nanosheets, particularly evident in the spectra collected at 16 and 20 hours. The corresponding FTIR spectra revealed that the C=C stretching vibration remained unchanged throughout this stage, indicating the preservation of robust coordination interactions between Ni and N moieties during reconstruction. After 16 hours of sonication, two broad bands emerged at 1300–1470 cm^{-1} and 1500–1730 cm^{-1}, characteristic of free TMAH, suggesting that TMAH molecules predominantly adsorbed on the surface of Ni-HITP nanosheets. This interpretation is further corroborated by the appearance of a weak O–H stretching vibration, implying the presence of surface-adsorbed TMAH species.

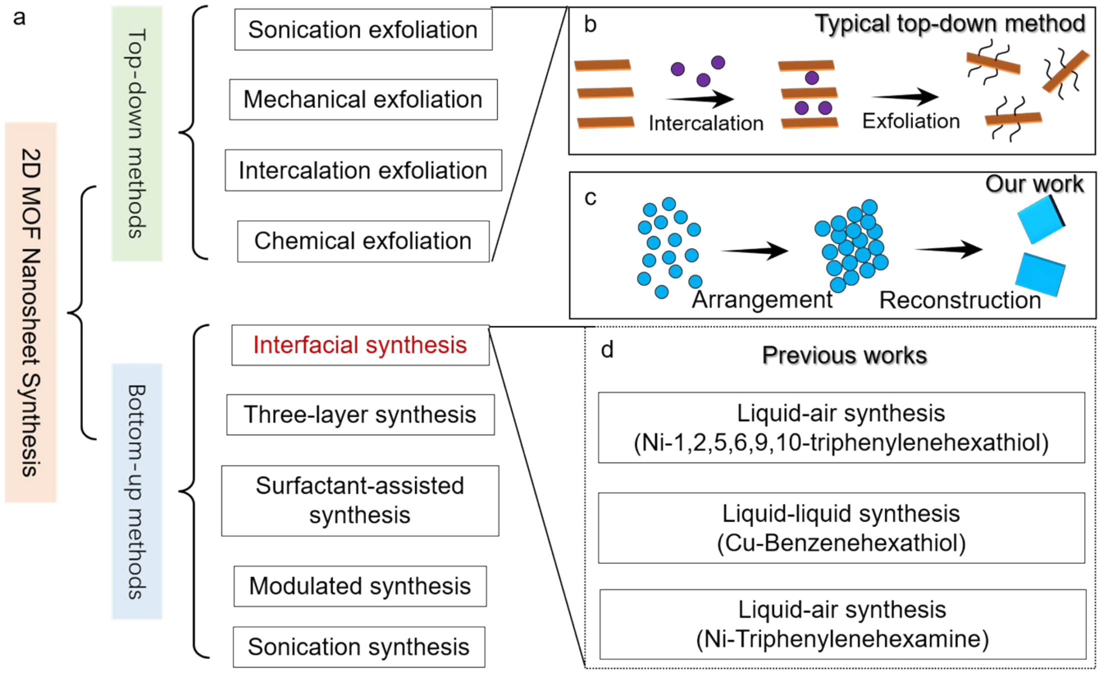

Figure S15. (a) Summary of the typical top-down and bottom-up methods for 2D MOF nanosheet synthesis. (b) The mechanism of the typical top-down method for 2D MOF nanosheet synthesis. (c) The arrangement-reconstruction process for 2D MOF nanosheet formation proposed by our work. (d) The synthesis methods for 2D MOF with HITP ligand or analogues.

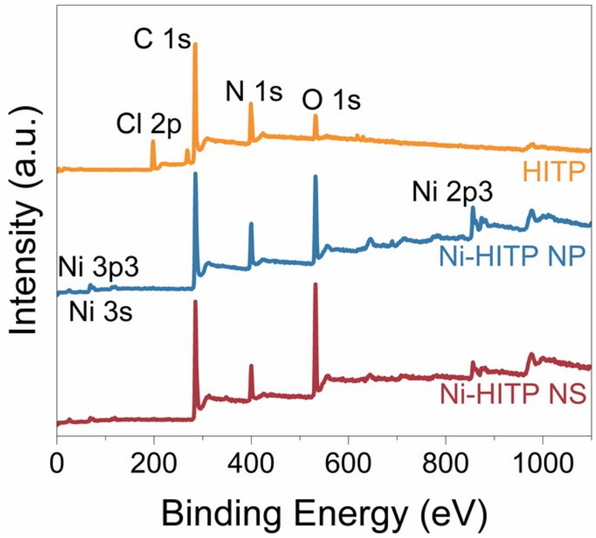

Figure S16. The full spectrum of HITP, Ni-HITP nanoparticles, and Ni-HITP nanosheets.

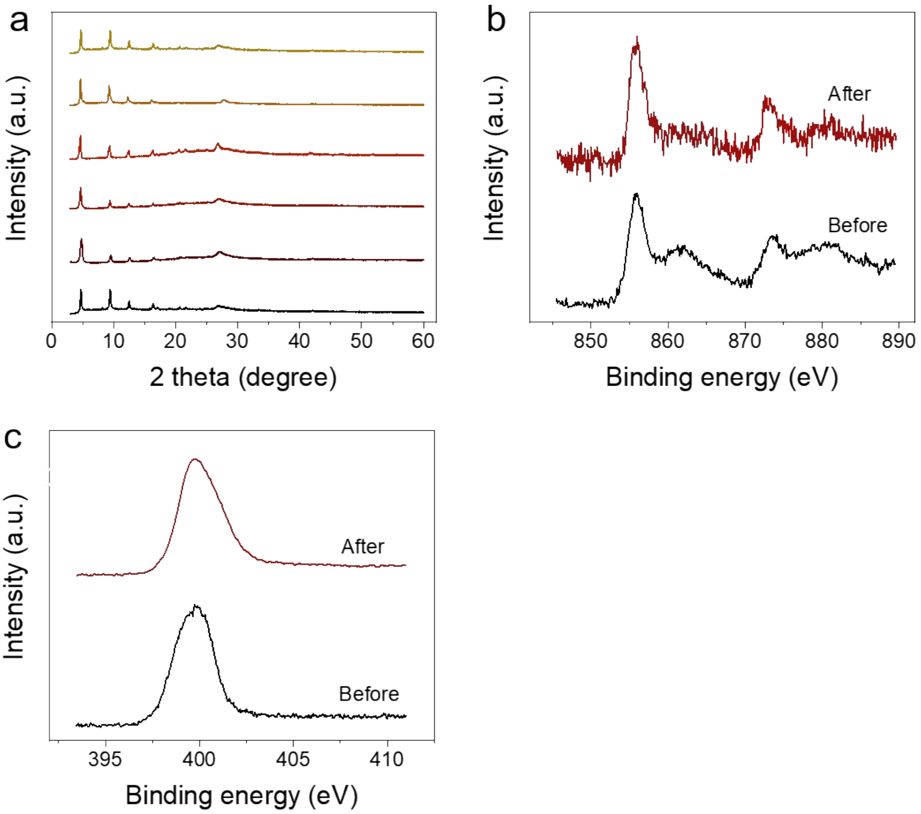

Figure S17. (a) The XRD patterns of Ni-HITP NS after soaking in 0.5 M H_2SO_4 for 12 h, 24 h, 36 h, 48 h, 60 h, and 84 h. The high-resolution XPS spectra of (b) Fe 2p, and (c) N 1s for pristine Ni-HITP NS and Ni-HITP NS after soaking in 0.5 M H_2SO_4 for 84 h.

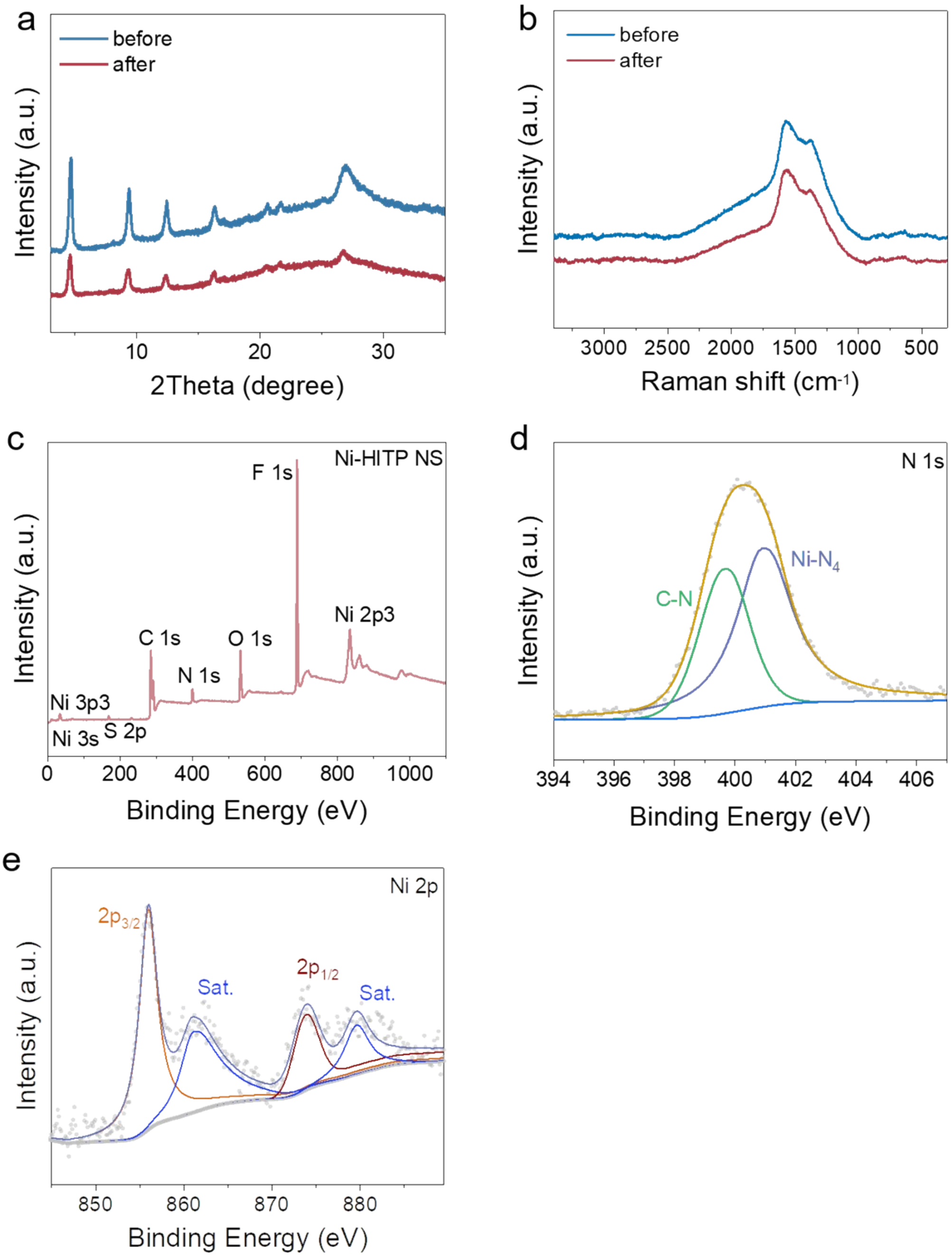

Figure S18. (a) XRD patterns, (b) Raman spectra of Ni-HITP NS before and after stability testing. (c) XPS full spectrum, (c) high-resolution N 1s, and (e) high-resolution Ni 2p spectrum.

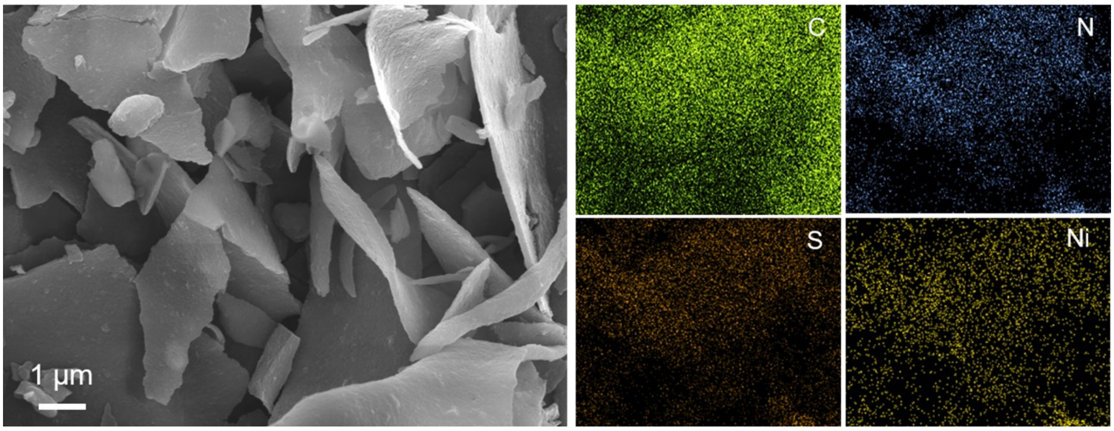

Figure S19. The SEM image of Ni-HITP NS after stability testing, and the corresponding EDS mapping of C, N, S, and Ni elements.

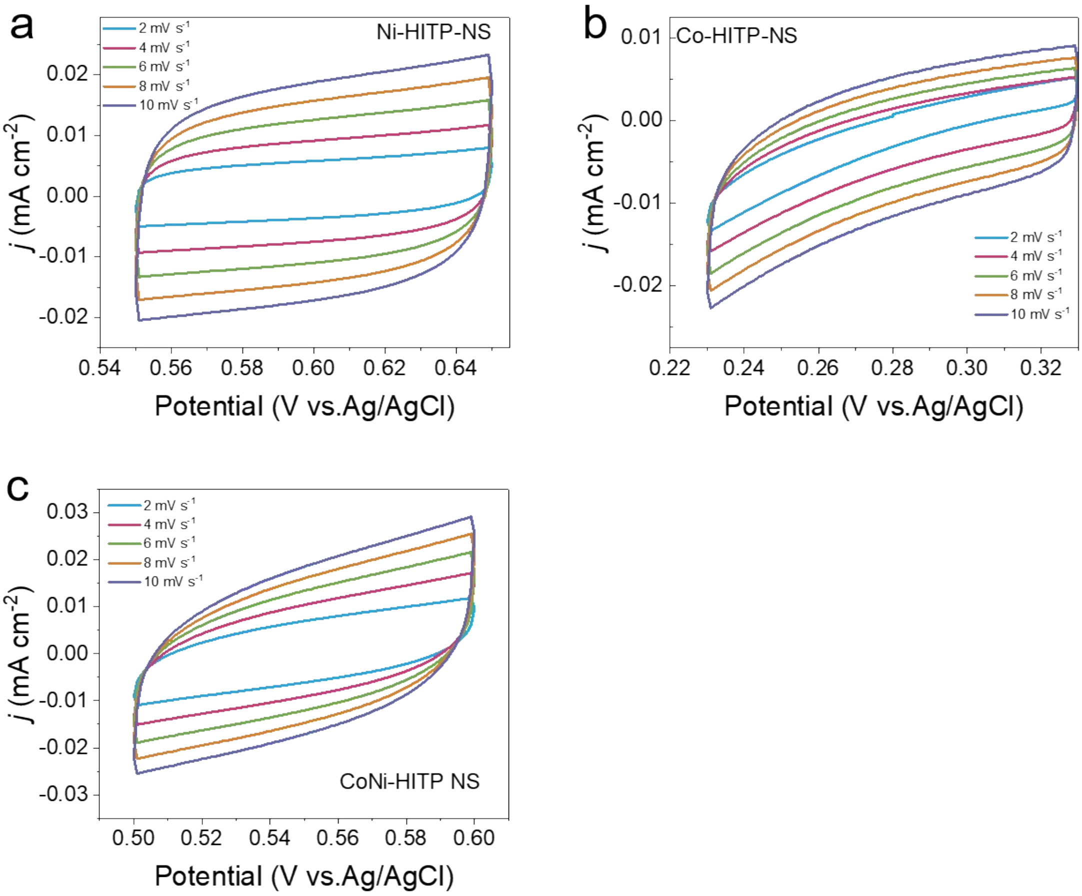

Figure S20. The CV curves of (a) Cu-HITP NP, (b) Fe-HITP NP, (c) Ni-HITP NP, (d) Zn-HITP NP, and (e) Co-HITP NP obtained in the non-Faradaic potential window.

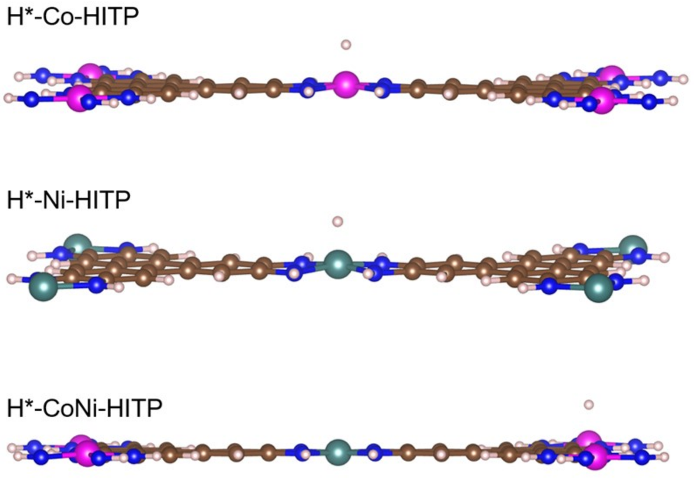

Figure S21. The adsorption models of H* on the Co-HITP, Ni-HITP, and CoNi-HITP.

References

1. J. Hafner. *J. Comput. Chem.*, 2008, **29(13)**, 2044-2078.

2. G. Kresse, J. Furthmüller. *Phys. Rev. B*, 1996, **54(16)**, 11169-11186.

3. P. E. Blöchl, C. J. Först, J. Schimpl. *Bull. Mater. Sci.*, 2003, **26(1)**, 33-41.

4. G. Kresse, D. Joubert. *Phys. Rev. B*, 1999, **59(3)**, 1758-1775.

5. J. P. Perdew, J. A. Chevary, S. H. Vosko, K. A. Jackson, M. R. Pederson, D. J. Singh, C. Fiolhais. *Phys. Rev. B*, 1992, **46(11)**, 6671-6687.

6. D. G. A. Smith, L. A. Burns, K. Patkowski, C. D. Sherrill. *J. Phys. Chem. Lett.*, 2016, **7(12)**, 2197-2203.

7. S. M. Rezwanul Islam, F. Khezeli, S. Ringe, C. Plaisance. *J. Chem. Phys.*, 2023, **159**, 234117-234140.

8. K. Momma, F. Lzumi. *Appl. Crys.*, 2008, **41(3)**, 653-658.